Orientational disorder drives site disorder in plastic ammonia hemihydrate - Supplemental Materials

Niccolò Avallone,* Simon Huppert,* Philippe Depondt,* Leon Andriambariarijaona,†
Frédéric Datchi,† Sandra Ninet,† Thomas Plé,‡ Riccardo Spezia,‡ and Fabio Finocchi*

I. COMPUTATIONAL DETAILS

Molecular Dynamics (MD) simulations have been performed via the Tinker-HP package for GPU architecture [1, 2]. The code is able to handle large numbers of molecules and it includes a variety of Force Fields (FFs). The FFs used in this study are the Optimized Potentials for Liquid Simulations All Atoms (OPLS-AA) [3, 4] for the ammonia molecules, and the Simple Point-Charge flexible (SPC/fw) [5], with parameters from Paesani et al. [6] for the water molecules. Periodic boundary conditions are applied, and long-range Coulomb interactions are handled using the Smooth Particle-Mesh Ewald algorithm [7]. In this study, we perform standard MD calculations in which the nuclei are treated as classical objects. Nuclear quantum effects are known to affect hydrogen bonds strength [8–10] and might therefore have an impact on the transition temperature that should be explored in future works.

The AHH-II structure at 300K and 3.5GPa, as experimentally determined by Wilson et al. [11] is monoclinic with an angle $\beta \sim 94.3°$. In order to construct an orthorhombic simulation box that approximates the AHH-II crystal structure, we proceed as follows: denoting a_u, b_u and c_u the experimental (monoclinic) unit cell vectors, the unit cell structure is first replicated 10 times along the b_u and c_u directions, and 30 times along the a_u direction. The simulation box vectors are thus defined as $a = 30a_u$, $b = 10b_u$ and $c = 10c_u + a_u$. In this way, a and c become almost perpendicular, so that neglecting the (very small) component of the c vector along the a direction yields an orthorhombic simulation box that closely approximates the AHH-II monoclinic structure. The final simulation box is shown in Figure 1 (the equivalent angle $\beta \sim 94.3°$ is visible in the x-z plane), it counts 12k water molecules, 24k ammonia molecules, for a total of 132k atoms. The structure was then optimized via the Tinker-HP structure optimization program to ensure a stable starting configuration for the molecular dynamics simulations.

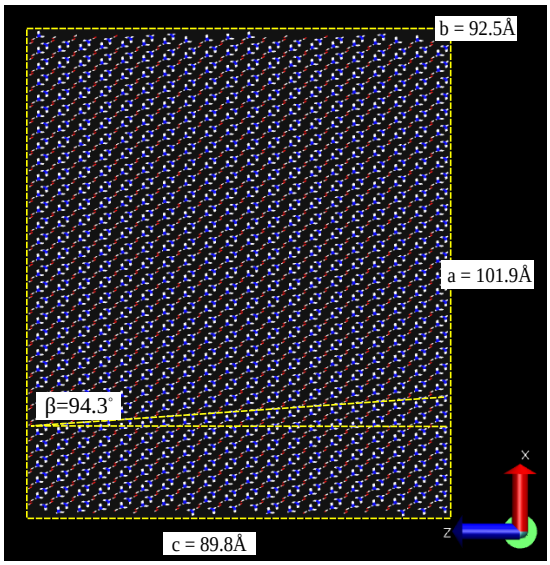

FIG. 1. Optimized AHH-II structure shown along the (0,1,0) direction in order to visualize the equivalent β angle of the monoclinic box. The three box dimensions (a, b, c) are also reported.

* Institut des NanoSciences de Paris (INSP), Sorbonne Université, CNRS UMR 7588, 75005 Paris, France
† Sorbonne Université, Muséum National d'Histoire Naturelle, CNRS UMR 7590, Institut de Minéralogie, de Physique des Matériaux et de Cosmochimie, IMPMC, 75005 Paris, France.
‡ Laboratoire de Chimie Théorique (LCT), CNRS and Sorbonne Université, 75005 Paris, France

For temperature control, we use a Langevin thermostat [12] with a system-bath coupling constant $\gamma = 20$ ps^{-1}. Time integration is performed through the BAOAB integrator[13] combined with the RESPA [14] multiple timestepping scheme (internal time step 0.25 fs, external one: 1 fs). For pressure control, we adopt the Langevin-piston barostat[15] in an anisotropic implementation: the box parameters in each direction are independently subject to a Langevin-Piston equation to ensure that the diagonal elements of the stress tensor fluctuate around the target pressure. The Langevin barostat has a coupling constant γ_V =20 ps^{-1} and the piston mass is chosen to guarantee a fast equilibration of the box parameters. The box angles were fixed to 90°, but, as explained above, the simulation box and the initial configuration are constructed to provide an orthorhombic approximant to the AHH-II monoclinic experimental structure (see Fig. 1).

The NPT molecular dynamics simulations at 6 GPa were performed in two different manners: either heating up the (previously optimized) AHH-II structure at the simulation temperature, or cooling down the AHH-pbcc structure (as obtained from MD simulations at 550 K). The duration of the trajectory is different for each temperature, depending on the time required for the system to equilibrate (see Section II), Table I summarizes the simulation times for all simulations at the pressure of 6 GPa. The other simulations, performed at higher or lower pressure (see Fig. 1 of the main text) correspond to heating trajectories, with a duration of about 10 ns per trajectory.

TABLE I. Simulation times for heating and cooling trajectories at different temperatures and a fixed pressure of 6 GPa. The starting configuration for the heating process is the (previously optimized) AHH-II structure, whereas the starting configuration for the cooling process is the 550K configuration obtained from the previous heating. For several temperatures (360, 370, 450, 550 and 600 K), we run solely simulations by starting from the equilibrium configuration at $T = 300$ K and heating.

T_{in}[K]	t_{sim}[ns] heating from 300K	t_{sim}[ns] cooled from 550K
300	10	5
350	15	5
360	37	–
370	15	–
380	18.5	5
390	33	5
400	30	10
450	10	–
500	30	10
550	19.2	—
600	10	–

Beside the NPT simulations with the friction parameter $\gamma = 20$ ps^{-1}, we also performed shorter (1ns) runs with a reduced friction parameter $\gamma = 0.1$ ps^{-1} to compute the diffusion coefficients. Moreover, in order to compute the dipole orientation autocorrelation functions and perform the hydrogen bond network (HBN) analysis, we performed 600 ps long NVT simulations. For these additional runs, the initial configuration was chosen as the final configuration explored in the NPT trajectories at the same temperature T, and the box parameters were fixed to their average value in the NPT runs. We also checked the dependence of the dipole and H-bond dynamics on the friction parameter γ, finding no significant variations between 20 ps^{-1} and 0.1 ps^{-1}.

In addition, to model X-ray diffraction patterns (see section III), we also run short (1 ns) simulations with the LAMMPS software (also on a GPU architecture) using a more general triclinic barostat [16]. These simulations make use of the generic NPT implementation of LAMMPS (including a Nosé-Hoover thermostat). No multiple timestepping technique is used and the time step is fixed to 0.5 fs.

II. PHASE TRANSITION MECHANISM

In this Section, we give some further details on the mechanism of the phase transition from the AHH-II crystal to the AHH-pbcc phase at high temperature, and on the methods used to highlight the transition in the simulations.

Figure 2 shows the average enthalpy (panel 2.a), volume (panel 2.b) and box parameters (panel 2.c) as a function of temperature, at a fixed pressure of 6 GPa and as obtained from the heating or from the cooling trajectories. From this data, the transition from AHH-II to AHH-pbcc is already visible (between 370 K and 400 K), as well as the melting point (between 550 K and 600 K). However, the transition temperature between AHH-II and AHH-pbcc is difficult to pinpoint precisely, as the enthalpy and the volume change relatively progressively with temperature upon heating, rather than experiencing a sudden discontinuity. We also clearly see that the transition is not reversible on the ns scale: once the disordered molecular alloy (DMA) phase is established at high temperature, it is preserved upon cooling. Indeed, the points obtained upon cooling tend to be all aligned on a straight line that coincides above

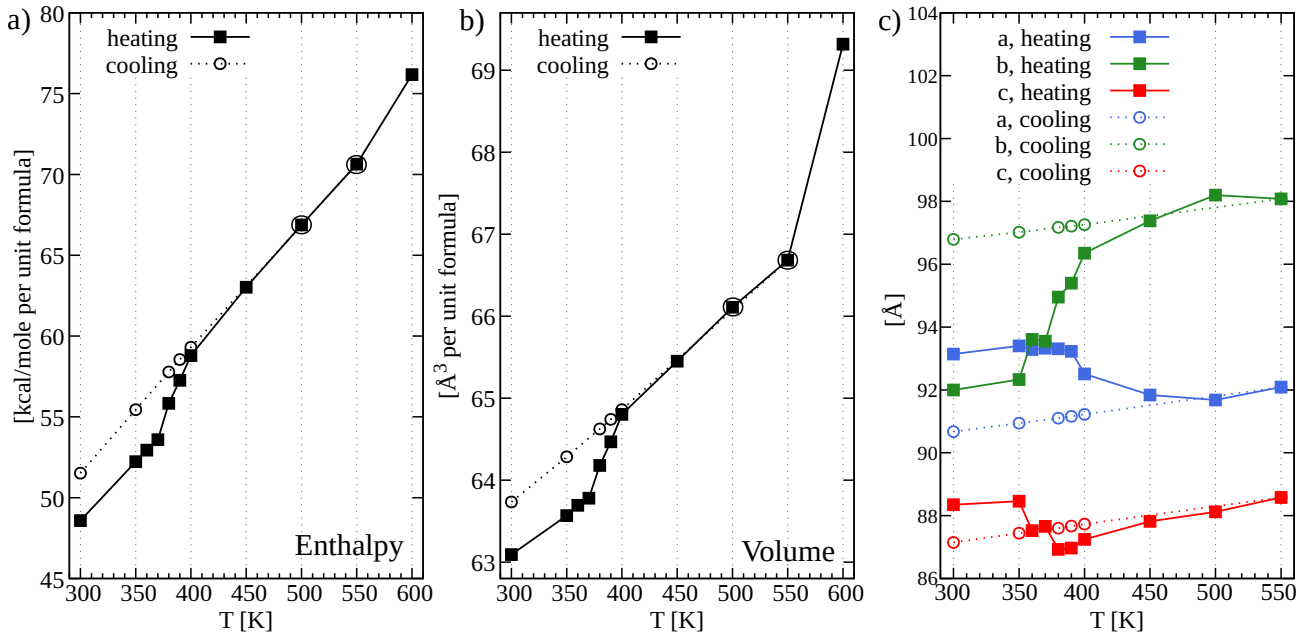

FIG. 2. Average enthalpy (panel a), volume (panel b) and box parameters (panel c) versus temperature, at 6 GPa pressure. The squares are obtained upon heating, starting from the AHH-II phase. The open circles have been obtained by cooling the AHH-pbcc structure as obtained from simulations at higher temperature (550 K).

400 K with the results obtained in the heating simulations. This is confirmed by the behavior of the individual box parameters (panel c): in the cooling process, the three parameters a, b and c have only a limited and monotonous dependence on temperature, with very similar slopes in all three directions, which suggests the preservation of an almost *bcc* structure at lower temperatures. On the contrary, in the heating process, the three parameters have very contrasted variations, with a and c decreasing as temperature increases from 350 K to 400 K, which is an evidence of a first order phase transition.

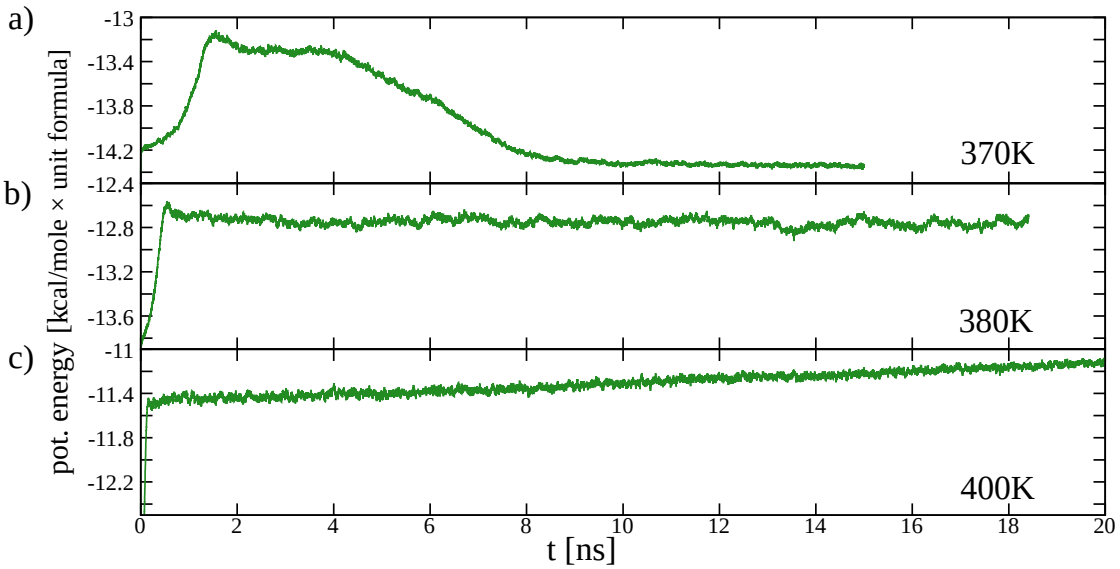

FIG. 3. Evolution of the potential energy for the trajectories at 6 GPa and temperatures of 370 K (a), 380 K (b) and 400 K (c), upon heating.

In order to determine the transition temperature more precisely, we show in Figure 3 the evolution of the potential energy (per unit formula) as a function of time, at 370 K (panel a), 380 K (panel b) and 400 K (panel c), upon heating.

x	y	z	atom	x	y	z
0.036	0.875	0.239	O	-0.018	0.880	0.257
0.137	0.785	0.183	H	-0.100	0.867	0.150
0.158	0.963	0.189	H	-0.115	0.956	0.307
0.716	0.133	0.416	N	0.714	0.129	0.413
0.418	0.145	0.402	H	0.406	0.146	0.401
0.775	0.031	0.370	H	0.821	0.215	0.370
0.783	0.129	0.534	H	0.792	0.133	0.528
0.667	0.882	0.900	N	0.665	0.865	0.885
0.370	0.896	0.888	H	0.360	0.886	0.870
0.726	0.781	0.853	H	0.751	0.966	0.840
0.741	0.876	0.017	H	0.745	0.875	-0.005

TABLE II. Wyckoff 4*e* positions corresponding to the AHH-II (left) and AHH-IIbis (right) crystal structures as obtained within the density functional theory (DFT) in the PBE approximation. The optimized lattice parameters at $T = 0$ K without zero-point effects are: $a = 3.407$ Å, $b = 9.004$ Å, $c = 8.599$ Å, $\beta = 93.65^\circ$ for the AHH-II configuration; $a = 3.364$ Å, $b = 9.756$ Å, $c = 8.054$ Å, $\beta = 88.32^\circ$ for the AHH-IIbis configuration. Both structures have $P2_1/c$ space group.

Below the transition temperature. In panel a), the energy increases in the first 2 ns of simulation, reaches a temporary plateau, then decreases smoothly until it finally stabilizes at a low value after approximately 8 ns of simulation. Figure 4 shows three partial snapshots along this trajectory, which explain this behavior: the system is initially ordered according to the AHH-II crystal structure, then experiences a transient orientational disorder (corresponding to the high-energy plateau), before it gradually reorganizes at longer times ($t > 8$ ns). By comparing the initial AHH-II structure to the final configuration, the positions of the O and N atoms are very similar, while the orientations of some hydrogen bonds clearly differ. From the final structure, we extracted the positions of the O and N atoms and constructed an alternative crystal network by optimizing a trial configuration for the H atoms. The resulting crystal, that we name AHH-IIbis, is about 0.18 kcal/mol higher in energy than AHH-II, within the PBE approximation of density functional theory (as obtained from structural optimization, *i.e.* at $T = 0$ K and without zero-point effects). Its structure differs from its AHH-II counterpart by the lattice parameters as well as by the position of some of the H atoms (see Table II). Visual inspection of the final configuration reached in the 370 K simulation (Fig. 3.a) shows that it consists in a mixture, with different domains corresponding either to the AHH-II or to the AHH-IIbis crystal. The AHH-IIbis structure is distinct from the AHH-II and almost degenerate in enegy (with comparable enthalpy within the chemical accuracy [17]). It likely shows up close to the transition to the plastic phase as a result of a partial "defreezing" of the rotational degrees of freedom.

The simulations show a similar behavior at 360 K, which contrasts to that at lower temperatures, where the AHH-II structure is stable during the dynamics. The average number of H-bonds of each type is unchanged between 350 K, where the initial AHH-II order is conserved over the whole simulation, and 370 K, where we observed the partial reorganization towards the AHH-IIbis structure (see Table IV). Furthermore, in the mixed configuration that is finally reached at 370 K, the molecular orientations remain stable over long times, as evidenced by the dipole decay curves presented in Fig. 3 of the main text. This shows that hydrogen bonds are still strong and lasting at this temperature, which prevents the molecular diffusion and the establishment of the DMA that characterizes the AHH-pbcc phase. Therefore, we assign the temperatures 370 K, 360 K and below to the ordered phases (either AHH-II or AHH-IIbis, that are almost degenerate in enthalpy).

Above the transition temperature. We obtain a completely different picture at 380 K (Figure 3.b): the potential energy increases rapidly and then remains stable for the rest of the simulation. Direct visual inspection of the system yields pictures similar to Fig. 4.b, with the presence of a strong and lasting orientational disorder. Therefore, we ascribe the 380 K simulations to the AHH-pbcc phase and locate the transition temperature T_c between 370 K and 380 K. Finally, at 400 K (Figure 3.c), after the sharp initial increase of the potential energy associated to orientational disordering, we observe a slower but steady increase. We attribute the latter to the molecular diffusion process which progressively leads to the DMA phase. Indeed, the potential energy (as well as the enthalpy and the volume) tends to converge towards the mean value obtained in the cooling trajectory at the same temperature, *i.e.* starting from a configuration in which the DMA is already fully established. We thus attribute the smooth transition observed in the enthalpy and volume evolution upon heating (Figure 2.a and 2.b respectively) between 380 K and 400 K to the finite duration of our MD runs. Indeed, at these temperatures, the molecular diffusion triggered by the orientational disorder is slow: at 380 K, it is not observed in the whole duration of the heating trajectory (though present in the cooling trajectory at the same temperature), and at 390 K, only few diffusion events occur in the heating simulation. Therefore the results presented in the main text for temperatures ranging from 380 K to 400 K are those obtained from cooling simulations (*i.e.* initiated from the AHH-pbcc structure at 550 K), in order to be representative of the equilibrium values that would be obtained in the long time limit.

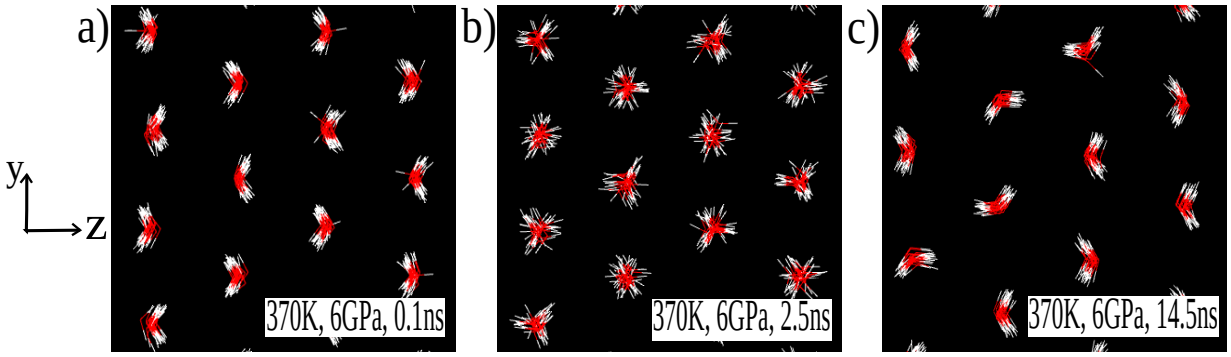

FIG. 4. Snapshot of a portion of the AHH simulated sample at 370 K and 6 GPa, after 0.1 ns (panel a), 2.5 ns (panel b) and 14.5 ns (panel c). Only water molecules are visible (oxygen in red, hydrogen in white), while ammonia molecules are hidden for clarity.

The same criterion is applied for the simulation results at pressures different from 6 GPa presented in the main article (Figure 1). For each point, a minimum of 5 ns of NPT simulation is performed, checking for one of the three possible types of evolution displayed in Figure 3. If the reordering process takes place, then the corresponding point in the phase diagram is assigned to the low-T AHH-II phase. Otherwise the (P,T)-point is associated to the AHH-pbcc phase. The simulation time is further extended in the cases in which the final configuration still shows an evolution that cannot be safely assigned to one or the other phase yet.

III. X-RAY DIFFRACTION PATTERNS

Figure 5 presents the X-ray diffraction (XRD) intensities obtained from the simulation trajectories at 6.9 GPa and temperature $T = 300$ K (panel a) and at 8.5 GPa and 433 K (panel b). The simulated XRD patterns are compared to experimental results from [18]. The simulated graphs agree with the experimentally observed phases, namely the plastic AHH-pbcc phase in panel b and the ordered AHH-II phase in panel a (see experimental phase diagram, Fig. 1.(a) of the main text for the localization of the different phases). We first note that, in the high temperature phase (panel b), both the experimental and the simulated XRD patterns display only few peaks, that neatly agree with those expected for a perfect bcc structure. The XRD intensity profile at low temperature is more complex (300 K, panel 5.a) and the various peaks are not as easily interpreted. However, most features observed in the experimental XRD pattern are well reproduced by the simulation, in particular the additional peaks at $2\theta \sim 9.5°$ and $2\theta \sim 11.5°$ and the triple peak feature at $2\theta \sim 15°$. In agreement with experiments, two short peaks are also visible at low angle ($2\theta \sim 5°$), that are absent from the high temperature XRD pattern. Only the broad feature between 8° and 9° is not perfectly captured, being a doublet in the simulated graph instead of the experimental triplet. The overall agreement between the experimental and simulation results confirms that, despite the simplicity of the interatomic interaction potential, the MD simulations capture the structure of the two phases with a very good accuracy.

The simulation XRD patterns were computed from 50 snapshots taken in the last 500 ps of the dynamics using the formula of the diffracted intensity:

$$I(\mathbf{q}) \propto \left| \sum_j f_j(|\mathbf{q}|) e^{i\mathbf{q}.\mathbf{R}_j} \right|^2$$

where the sum runs over all the atomic indices j and $\mathbf{q}$ is a vector of the reciprocal lattice of the periodic simulation box. As the experimental samples are poly-crystalline the XRD intensity at a given diffraction angle 2θ is obtained by summing over all the corresponding reciprocal lattice vectors $\mathbf{q}$ such that $\sin(\theta) = \lambda|\mathbf{q}|/4\pi$, then multiplying by the geometric Lorentz-polarization factor (see for instance Ref. 19):

$$L_p(\theta) = \frac{1 + \cos^2(2\theta)}{\cos\theta \sin^2\theta}$$

To simplify the calculation, given the large number of atoms in our simulations, we neglected the hydrogen form factor f_H while, $f_O(|\mathbf{q}|)$ and $f_N(|\mathbf{q}|)$ being very similar, we used the same averaged form factor for both oxygen and nitrogen atoms.

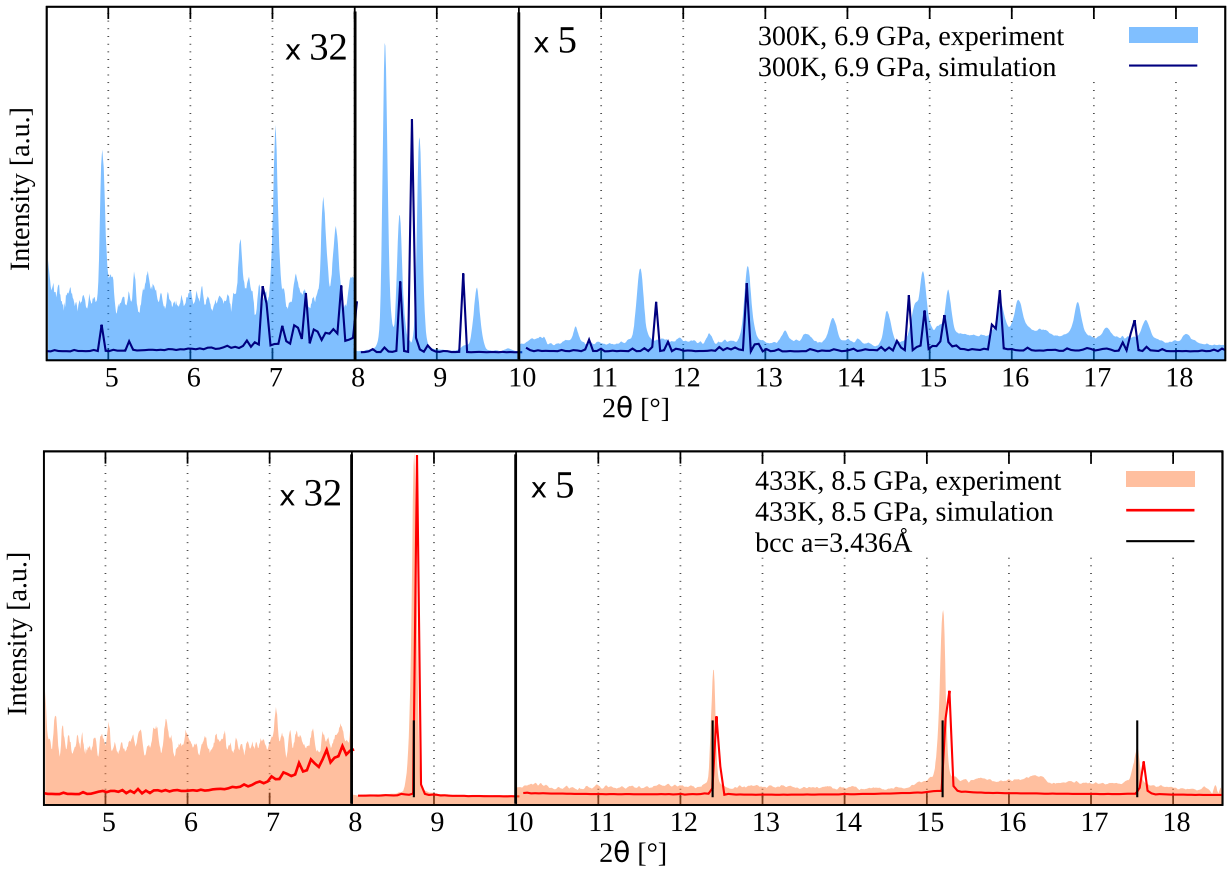

FIG. 5. X-ray diffraction intensities at wavelength $\lambda = 0.3738$ Å, as obtained from MD simulations (using a triclinic barostat, see section IV below) and compared with the experimental results from [18]. Intensities (in arbitrary units) are multiplied by a factor 32 at low angles ($2\theta < 8°$), and by a factor 5 at high angles ($2\theta > 10°$), for visualization purposes. The two panels represent the two phases under study: AHH-II in panel a and AHH-pbcc in panel b. In the high-temperature phase (panel b), the vertical sticks represent the position of the diffraction peaks expected for a perfect bcc crystal with the experimental value of the cubic lattice parameter a.

IV. SHAPE OF THE SIMULATION BOX

The results presented in the main text were obtained using an anisotropic Langevin barostat, that allows only for orthorhombic deformations of the simulation box: the box parameters along x, y and z vary independently in such a way to guarantee that the pressure in all three directions fluctuates around its target value, but the box angles remain fixed at 90°. In contrast, the XRD patterns presented in Fig. 5 were obtained from additional simulations performed with a fully triclinic barostat that allows to relax the constraint on the box angles. These relatively short (1 ns) additional runs were performed with the LAMMPS software [16] as Tinker-HP, used in the rest of this study, does not include such a triclinic barostat. The simulation set-up is otherwise similar and the initial configuration of the system was set to the final configuration reached in the simulations with the orthorhombic barostat.

Figure 6 compares the XRD intensities computed from simulations with the triclinic (blue curves) and with the orthorhombic (red curves) barostat. The simulations were performed at 6 GPa and at two different temperatures: 300 K and 500 K, corresponding to the AHH-II and AHH-pbcc phases respectively. In the low temperature phase (300 K, panel b), the results are almost superimposed. Indeed, the orthorhombic simulation box was constructed as an approximant to the monoclinic structure of the low-temperature AHH-II phase. Therefore, when a triclinic barostat is used, the box angles remain very close to 90° (only β is slightly reduced to $\sim 89.6°$). In contrast, at 500 K, the angle β varies more significantly, falling down to $\sim 86.1°$ (angles α and γ remain essentially unchanged). The reduction of the angle β is important to recover a perfect bcc structure for the high-temperature phase, as illustrated in Fig. 6.a: in the simulations with the orthorhombic box (red line), the bcc diffraction peaks tend to become doublets due to the constraint imposed on the β angle.

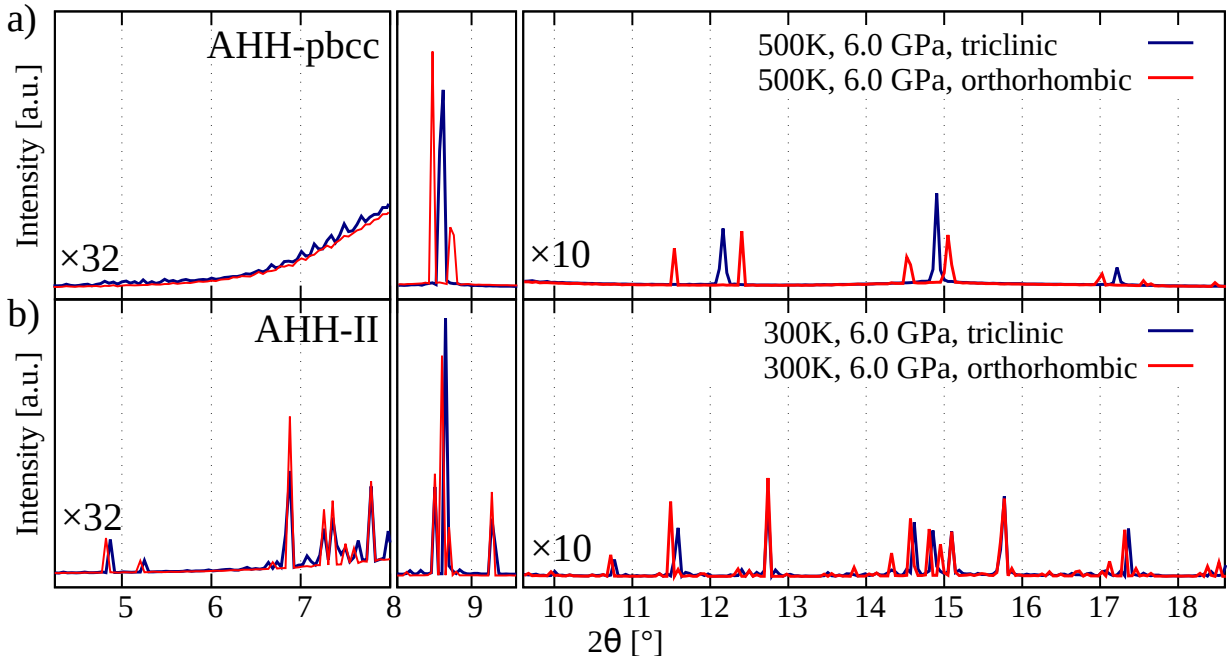

FIG. 6. X-ray diffraction intensities from NPT simulations using the triclinic barostat (via LAMMPS) compared with the results obtained in an orthorhombic simulation box (via Tinker-HP), for the two phases: AHH-II in panel b, AHH-pbcc in panel a. Intensities (in arbitrary units) are multiplied by a factor 32 at low angles ($2\theta < 8°$), and by a factor 10 at high angles ($2\theta > 9.5°$), for visualization purposes.

Though the angular constraint can affect macroscopic observables such as the XRD patterns, it likely has little effect on the microscopic mechanisms of the phase transition that are analyzed in details in the main text. In particular, the orientational-disorder-driven site disorder (ODDSD) phenomenon, which stems from the breaking of hydrogen bonds and the subsequent atom rearrangements, is mostly a local phenomenon, that depends on the short- and medium-range order but is little affected by the orthorhombic shape of the simulation box. As a check, we performed additional simulations at 6GPa and different temperatures using the triclinic barostat (via LAMMPS). In these runs, the process illustrated in Fig. 3.a, *i.e.* transient orientational disorder followed by gradual reorganization, is already observed at 350 K, while no sign of reorganization is visible after 8 ns at 360 K and 370 K. This suggests that, while the precise value of T_C might slightly change (by 20 K at most) when adopting orthorhombic or triclinic boundary conditions, the microscopic mechanism of the phase transition, namely ODDSD, is not affected.

V. ORIENTATIONAL DISORDER

Figure 3 of the main article shows the decay of the dipole orientation autocorrelation functions $\langle \mathbf{u}_i(0)\mathbf{u}_i(t)\rangle$ for temperatures above and below T_c. The curves are computed from NVT runs of 600 ps after full equilibration, i.e. starting from the final configuration reached in the NPT simulations, either in heating or in cooling depending on whether the temperature is below or above T_c. No significant dependence on the thermostat friction γ was found. The decay of the correlation functions can be fitted with an exponential $B\,\mathrm{e}^{-\frac{t}{\tau}} + C$, letting aside the very short times ($t < 1$ps) which involve mainly librational motion, not molecular re-orientations. Table III displays the corresponding correlation times $\tau(T)$ and saturation constants $C(T)$. Two distinct regimes can be observed. Below T_c, the correlation times $\tau(T)$ are larger than 50 ps and C is almost 1, revealing persistent molecular orientations. At T_c, the sharp decrease of one order of magnitude of τ to less than 10 ps and the drop of C to ~ 0 show that both H_2O and NH_3 loose memory of their orientations on the ps time scale, which is characteristic of the plastic AHH-pbcc phase.

TABLE III. Water and ammonia dipole correlation times $\tau(T)$ and saturation constants $C(T)$ at different temperatures and fixed pressure of 6GPa, obtained from the exponential decay fit of the dipole orientation autocorrelation function $\langle \mathbf{u}_i(0)\mathbf{u}_i(t)\rangle$.

$T_{in}[K]$	τ^{H_2O} [ps]	τ^{NH_3} [ps]	$C(T)^{H_2O}$	$C(T)^{NH_3}$
300	> 500	> 500	0.955	0.926
350	70	58	0.913	0.881
360	78	74	0.873	0.844
370	51	47	0.908	0.866
380	4.7	3.9	0.009	0.017
390	4.2	3.4	0.011	0.015
400	2.5	2.3	0.009	0.013
500	1.1	0.9	0.003	0.005
550	0.4	1.4	0.001	0.001
600	0.8	0.5	0.000	0.000

VI. HYDROGEN BOND NETWORK

In Table IV, we collect the average number of hydrogen bonds for various temperatures at $P = 6$ GPa (they are of four different types, considering that each molecule – water or ammonia – can donate or accept an H-bond). These numbers are obtained according to the existence criterion defined by Luzar and Chandler [20] for H-bonds, which combine a donor-acceptor distance cutoff r_{cut} and an angular cutoff θ_{cut}. The first line of the table shows the number of hydrogen bonds in the ideal AHH-II structure (as taken from Wilson *et al.* [11]). These numbers are essentially conserved below the critical temperature T_c at which a sharp change is clearly observed. Indeed, the plastic phase is characterized by an increased number of homo-molecular H-bonds which only partially compensates the reduction in the number of hetero-nuclear bonds. The plastic H-bond network is therefore significantly looser than its crystal counterpart. Indeed, in AHH-pbcc, the average number of each type of hydrogen bond is only slightly superior to that observed in the liquid mixture at 600 K.

TABLE IV. Number of hydrogen bonds versus temperature, normalized to the number of donors X (X = N or O). The cutoff donor-acceptance distance for the existence of a H-bond is set to $r_{cut} = 3.5$ Å and the angular cutoff to $\theta_{cut} = 30°$ [20].

$T_{in}[K]$	$n_{OH\ldots O}$	$n_{NH\ldots N}$	$n_{NH\ldots O}$	$n_{OH\ldots N}$
0	0	1	2	2
300	0.00(0)	1.07	1.81	1.99
350	0.01	1.11	1.68	1.97
360	0.02	1.11	1.69	1.96
370	0.02	1.12	1.66	1.96
380	0.64	1.61	0.96	1.20
390	0.63	1.59	0.97	1.20
400	0.64	1.59	0.95	1.18
500	0.59	1.47	0.93	1.16
600	0.66	1.34	0.81	1.05

In the main article, we report the hydrogen bond lifetimes for various temperatures and for each molecular type. They are obtained from an exponential fit of the decay time of the normalized number of hydrogen bonds, which are shown in Figure 7. These curves are obtained from 600 ps long NVT simulations, performed after full NPT equilibration at 6 GPa (simulation times in Table I). The curves start from the normalized number of H-bonds reported in Table IV. The decay curves are obtained with the following method: at each simulation time frame, the number of surviving H-bonds is estimated. If a bond does not fulfill the Luzar and Chandler criterion [20] at time t', the bond is considered broken and it will not contribute to the longer time $t > t'$ count. As temperature increases, the decay of hydrogen bonds in which nitrogen is the donor becomes faster but without a clear distinction between the low temperature and the high temperature phases. On the contrary, a clear transition is visible for H-bonds involving oxygen as the donor. In panel b, the decay of OH$\cdots$N bonds is slow at low temperatures, and suddenly becomes significantly faster at $T = 380$ K and above. In parallel, in panel d, the number of OH$\cdots$O bonds (essentially absent at low temperature) suddenly increases at 380 K. It then shows a fast exponential decay as a function of time, at all temperatures above T_c.

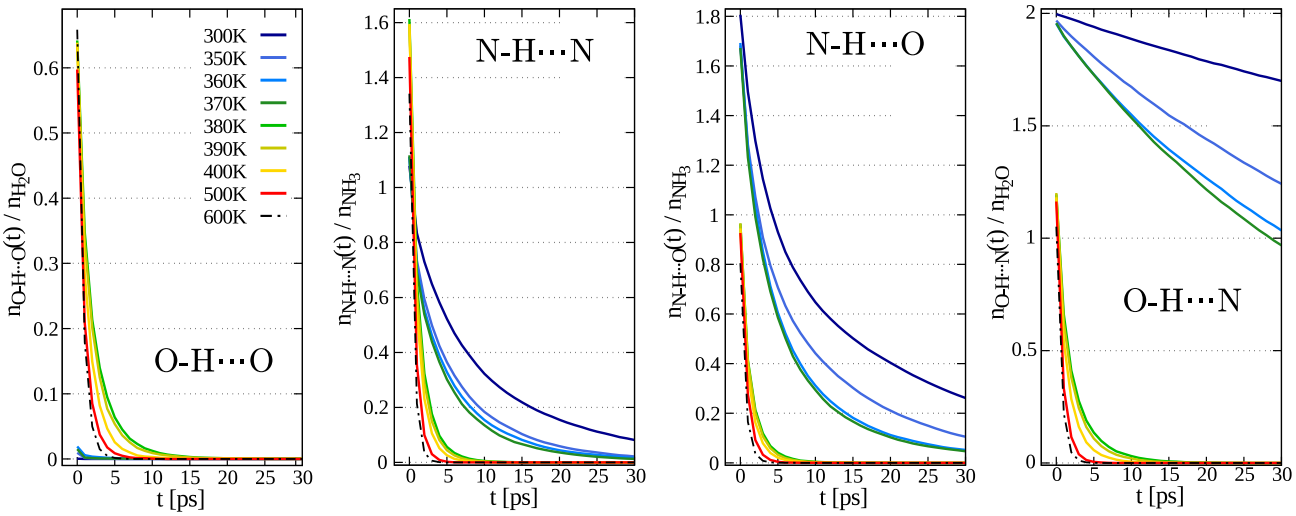

FIG. 7. Hydrogen bond number $n_{XH...Y}(t)$ as function of time. The cutoff donor-acceptance distance for the existence of an H-bond is set to $r_{cut} = 3.5$ Å and the angular cutoff to $\theta_{cut} = 30°$ [20].

[1] L. Lagardère, L.-H. Jolly, F. Lipparini, F. Aviat, B. Stamm, Z. F. Jing, M. Harger, H. Torabifard, G. A. Cisneros, M. J. Schnieders, N. Gresh, Y. Maday, P. Y. Ren, J. W. Ponder, and J.-P. Piquemal, Chem. Sci. **9**, 956 (2018).

[2] O. Adjoua, L. Lagardère, L. H. Jolly, A. Durocher, T. Very, I. Dupays, Z. Wang, T. J. Inizan, F. Cèlerse, P. Ren, J. W. Ponder, and J. P. Piquemal, J. Chem. Theory. Comp. **17**, 2034 (2021).

[3] W. L. Jorgensen and J. Tirado-Rives, J. Am. Chem. Soc. **110**, 1657 (1988).

[4] W. L. Jorgensen, D. S. Maxwell, and J. Tirado-Rives, J. Am. Chem. Soc. **118**, 11225 (1996).

[5] Y. Wu, H. L. Tepper, and G. A. Voth, J. Chem. Phys. **124**, 024503 (2006).

[6] F. Paesani, W. Zhang, D. A. Case, T. E. Cheatham, and G. A. Voth, J. Chem. Phys. **125**, 184507 (2006).

[7] U. Essmann, L. Perera, M. L. Berkowitz, T. Darden, H. Lee, and L. G. Pedersen, J. Chem. Phys. **103**, 8577 (1995).

[8] X.-Z. Li, B. Walker, and A. Michaelides, Proc. Natl. Acad. Sci. U.S.A. **108**, 6369 (2011).

[9] S. Huppert, T. Plé, S. Bonella, P. Depondt, and F. Finocchi, Simulation of nuclear quantum effects in condensed matter systems via quantum baths, Appl. Sci. **12**, 4756 (2022).

[10] S. Schaack, E. Mangaud, E. Fallacara, S. Huppert, P. Depondt, and F. Finocchi, When quantum fluctuations meet structural instabilities: the isotope-and pressure-induced phase transition in the quantum paraelectric naoh, Phys. Rev. Lett. **131**, 126101 (2023).

[11] C. W. Wilson, C. L. Bull, G. Stinton, and J. S. Loveday, J. Chem. Phys. **136**, 094506 (2012).

[12] B. Leimkuhler and C. Matthews, J. Chem. Phys. **138**, 174102 (2013).

[13] B. Leimkuhler and C. Matthews, Proc. R. Soc. A. **472**, 0138 (2016).

[14] M. Tuckerman, B. J. Berne, and G. J. Martyna, J. Chem. Phys. **97**, 1990 (1992).

[15] S. E. Feller, Y. Zhang, R. W. Pastor, and B. R. Brooks, J. Chem. Phys. **103**, 4613 (1995).

[16] A. P. Thompson, H. M. Aktulga, R. Berger, D. S. Bolintineanu, W. M. Brown, P. S. Crozier, P. J. in 't Veld, A. Kohlmeyer, S. G. Moore, T. D. Nguyen, R. Shan, M. J. Stevens, J. Tranchida, C. Trott, and S. J. Plimpton, Comput. Phys. Commun. **271**, 108171 (2022).

[17] The enthalpy difference per unit formula between the AHH-IIbis and the AHH-II is +0.18 kcal/mol at $T = 0$ K and $P = 5$ GPa within the DFT and about -0.4 kcal/mol at $T = 300$ K and $P = 6$ GPa using the empirical force fields OPLS-AA and SPC/Fw and the monoclinic barostat available in LAMMPS (as described in section IV), in order to allow for the relaxation of the crystal angles between the two structures.

[18] L. Andriambariarijaona, F. Datchi, H. Zhang, K. Béneut, B. Baptiste, N. Guignot, and S. Ninet, Phys. Rev. B **108**, 174102 (2023).

[19] S. Coleman, D. Spearot, and L. Capolungo, Model. Simul. Mat. Sci. Eng. **21**, 055020 (2013).

[20] A. Luzar and D. Chandler, Nature **379**, 55 (1996).